



Use of In Situ SEM Multiple Cracking Test to Correlate Crack Propagation Mode with Acoustic Emission Signals in Thermal Oxide Scales: Application to Ni/NiO System

S. Houde^{1,2} · J. Marteau¹ · J. Favergeon¹

Received: 9 July 2024 / Revised: 11 July 2024 / Accepted: 20 July 2024

© The Author(s), under exclusive licence to Springer Science+Business Media, LLC, part of Springer Nature 2024

Abstract

Multicracking tests are carried out in an SEM on nickel specimens preoxidized at high temperature. These tests are monitored by acoustic emission. By combining the analysis of the acoustic emission signals with SEM observations of the specimens, it is possible to find the signatures of the two active crack propagation modes. In mode I (propagation perpendicular to the metal–oxide interface), the acoustic emission signals have high amplitudes and short durations, whereas for propagation in mode II (along the metal–oxide interface), the AE signals have low amplitudes and long durations.

Keywords High-temperature oxidation · Acoustic emission · Crack propagation

Introduction

Mechanical resistance and adhesion of oxide scales on substrate are of primary importance to ensure the reliability of their protective effects. To better manage the performance of these systems, it is necessary to assess the mechanical resistance of scales on substrate in order to better understand thin scale/substrate failure

✉ J. Favergeon
jerome.favergeon@utc.fr

S. Houde
solene.houde@arcelormittal.com

J. Marteau
Julie.marteau@utc.fr

¹ Université de technologie de Compiègne, Roberval (Mechanics Energy and Electricity), Centre de recherche Royallieu - CS 60 319, 60203 Compiègne Cedex, France

² ArcelorMittal Global Research and Development, Route de Saint Leu, 60100 Montataire, France

mechanism. Several studies coupled mechanical testing (tensile or bending tests) with acoustic emission (AE). This technique is based on the use of sensors to detect transient elastic waves generated by irreversible changes occurring inside a material (plastic deformations, crack nucleation and propagation, corrosion, etc.). However, it should be underlined that acoustic activity is the result of wave propagation through the material to the surface, which can modify the wave characteristics. Thus acoustic activity is highly dependent on the examined material deformation but also on the material history (type of material, metallurgical history and resulting microstructure, strain level, etc.) as well as on acoustic emission test conditions.

Different strategies were used to try and correlate recorded AE events with the investigated phenomena. Clustering of acoustic signals can be performed through the k-mean clustering method [1] or principal component analysis [2, 3]. However, these clustering methods were most often dedicated to the study of the behavior of composite materials, which are particularly emissive. Another strategy consists in examining the frequency response of AE signals. Huang et al. [4] used a frequency analysis to identify the mechanisms taking place during tensile testing of steam-side oxide scales formed on steel. They identified three frequency bands during the test respectively corresponding to the plastic deformation of the substrate, scale cracking and scale spalling. Table 1 presents an overview of tensile or bending tests coupled with AE that were used to characterize thin film/substrate systems. It shows that AE parameters were often used to characterize AE signals without the use of clustering. Other than the frequency, the most used parameters were: the energy [5–10], the amplitude [4, 5, 9–11] and the number of events [4, 5, 7, 10, 12, 13]. Sometimes, event positions [5] or a qualitative description of the waveform [14] was also used.

In the framework of multiple cracking testing, some correlations were established between AE signatures and the investigated phenomena. At first, AE was only used to confirm first cracking occurrence [13]. Then, Hall et al. [14], through the bending of oxidized mild steel, managed to identify two different types of waveforms and to correlate them to scale fracture either in tension (through scale) or in compression (decohesion). Nagl et al. [7] tried to correlate the number of observed cracks with the number of recorded AE signals. They also linked the number of spalled segments with AE events having high energy. Bruns et al. [5] coupled the observations of AE energy through time with the examination of transverse sections of nickel oxides and identified two signal clusters corresponding to either the beginning of the disintegration of the outer layer of the oxide or the formation of through-scale cracks. However, the examination of the AE parameters did not lead to identify discriminating characteristics ensuring an easy classification of the signals. This small overview of the literature highlights the difficulty in linking mechanisms to specific AE signals and the lack of “universal” correlations.

In this study, multiple cracking tests were conducted inside a scanning electron microscope (SEM) equipped with AE system to correlate crack propagation modes with acoustic signals. The Ni/NiO system was chosen as the application system.

Table 1 Overview of AE parameters used in tensile/bending tests performed on thin film/substrate systems

References	Material	Test type	AE parameters
[12]	Plasma-sprayed coating on steel	4-point bending test	AE amplitude distribution, number of events
[5]	Oxide scales on Ni and TiAl	4-point bending test	Number of events, energy, amplitude, hit number, mean frequency, event location
[14]	Oxides on mild steel	3-point bending test	Waveform
[4]	Steam-side oxides on steel	Tensile test	Amplitude, number of events, frequency
[6]	TiN coatings on stainless steel	Tensile test	Signal envelope, energy, median frequency
[7]	Iron and nickel oxide scales	4-point bending test	Number of events, energy
[8]	Thermal barrier coating	4-point bending test	Cumulated energy
[9]	Oxides on steel	4-point bending test	Amplitude, energy
[13]	Oxides on steel and nickel 99.6	Tensile test	Number of events
[10]	Thermal barrier coating	Tensile test	Number of events, number of hits, energy, amplitude, frequencies
[11]	Tungsten coatings on steel	Tensile test	Amplitude, shape factor (ratio of the maximum amplitude to the efficient value)

Experimental Procedures

Tensile specimens having a gauge length of 15 mm and a width of 2 mm were waterjet cut from laminated sheets of commercially pure nickel (99.8%) having a thickness of 1 mm (Goodfellow). Table 2 shows the chemical composition of the nickel sheet.

Two different oxidation conditions were used to obtain different oxide scale thicknesses and characteristics. Four specimens were oxidized in a muffle furnace at 550 °C under laboratory air for 30 h to obtain porous oxide scales having a thickness of $1.4 \pm 0.4 \mu\text{m}$. Four other specimens were oxidized at 900 °C for 2 h to develop porous oxide scales having a thickness of $6.3 \pm 1.4 \mu\text{m}$. For the sake of brevity, the first oxide thickness is hereafter referred as Ni/NiO-1 μm while the second is called Ni/NiO-6 μm .

Tensile tests were performed with Proxima 100 testing stage (microMECHA, Germany) equipped with a load cell of 3000 N (linearity of ± 15 N and hysteresis of ± 15 N). The displacement resolution was 20 nm with a displacement speed of the moving grip of 1 $\mu\text{m/s}$. Force and displacement were measured; stress was calculated from the force values using the initial section of the specimen gauge, and strain was calculated from the measured displacement using the initial gauge length, applying a correction that takes into account the stiffness of the traction platform. For each configuration (no oxide and two different oxide thicknesses), three continuous tests were performed with AE monitoring. Additionally, for each examined oxide scale thickness, an additional test was done to take SEM pictures of the oxide at different stages of deformation. SEM images were taken with a field emission SEM Zeiss Sigma™ using secondary electron detector.

The acoustic emission system was designed by Mistras Group SAS (France). Two PICO sensors were glued to the specimen heads with a distance between sensors equal to 41 mm. The used PICO sensors had good sensitivity for frequencies comprised between 200 and 750 kHz. These sensors were linked to the acquisition setup through preamplifiers having a gain of 40 dB and fitted with band-pass filtering (200 to 1000 kHz). Data were recorded with AE Win software using a 30 dB threshold and were then treated using Noesis© software.

Before each test, AE sensors were checked with 0.5 mm *Hsu-Nielsen* pencil lead break (NF EN 1330-9 [15]). After each test, AE signals caused by instrumental noise were removed: They corresponded to signals having an amplitude lower than 30 dB. Then, only the signals located inside the gauge length, i.e., signals situated at a distance larger than 4 mm to the sensors were kept for the analysis.

Table 2 Chemical composition of the nickel sheets (Goodfellow data)

Element (ppm)	Co	Cr	Cu	Fe	Mg	Mn	Si	Ti	C	S
Ni sheets	8	8	10	10	10	10	8	10	70	10

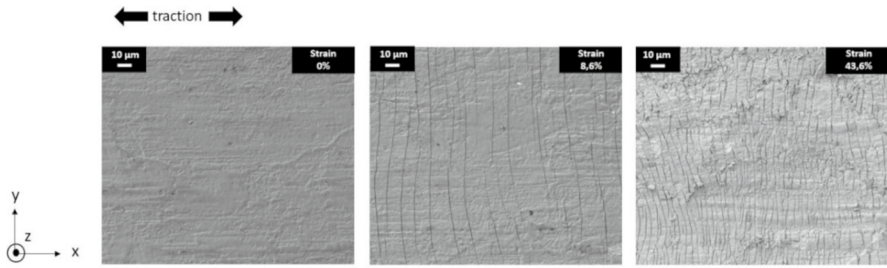


Fig. 1 SEM images of multiple cracking test—Ni/NiO-1 μm

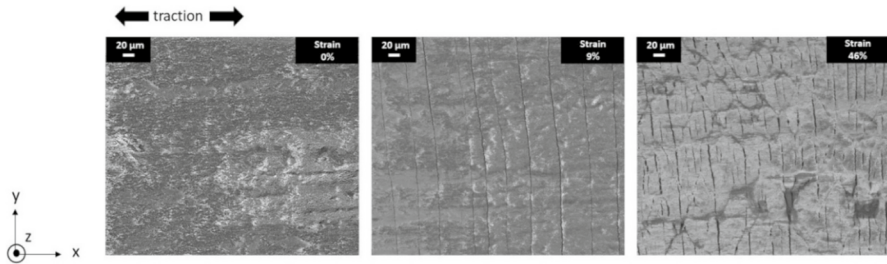


Fig. 2 SEM images of multiple cracking test—Ni/NiO-6 μm

Multiple Cracking Test Results and SEM Observations

Discontinuous tensile tests were performed on Ni/NiO-1 μm and Ni/NiO-6 μm to observe oxide cracking and possible spalling (note that when the test is stopped, stress relaxation occurs). For Ni/NiO-1 μm , thanks to SEM observations, the first crack was noticed for a deformation of 2.1% and spalling occurred from a deformation of 8.6% until the end of the test. No new crack appeared after a deformation of 11.6%, and the minimum inter-crack distance is found to be equal to 6 μm (Fig. 1). For Ni/NiO-6 μm , the first crack was discerned for a deformation of 1.9%. No spalling was detected. The last cracks emerged on the surface at a deformation of 9%, and the minimum inter-crack distance is equal to 35 μm (Fig. 2).

The evolutions of mean crack spacing with imposed strain are given in Fig. 3 for both nickel oxide thicknesses. The results show the same tendencies as ever reported in the literature for different substrate/coating couples [11, 16–20]: The distance between consecutive cracks decreases rapidly with increasing strain and stabilizes at an asymptotic value (saturation distance, D_{sat}); moreover, the D_{sat} value increases with oxide thickness. This last observation has been extensively explained with different models [21–24].

After fracture, cross sections of the specimens were observed to analyze the crack morphologies (Fig. 4). Different types of cracks were observed and are highlighted in the images:

- Large through-scale cracks that can be qualified as opened cracks,

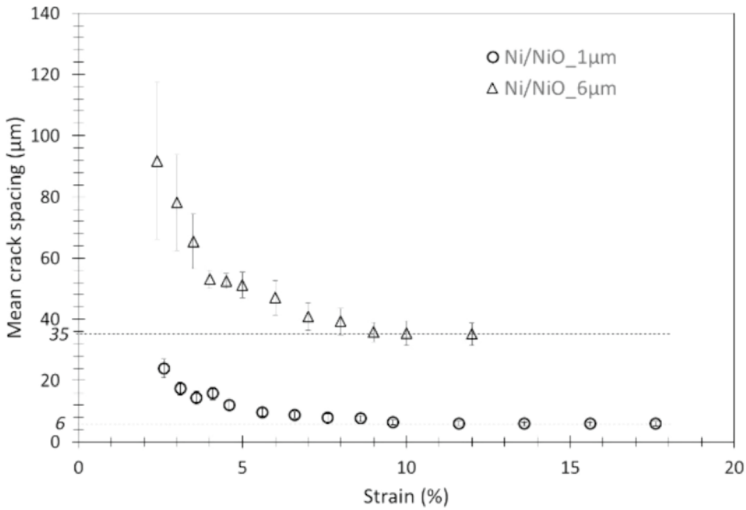


Fig. 3 Evolution of the mean crack spacing with applied strain for Ni/NiO-1 μm and Ni/NiO-6 μm

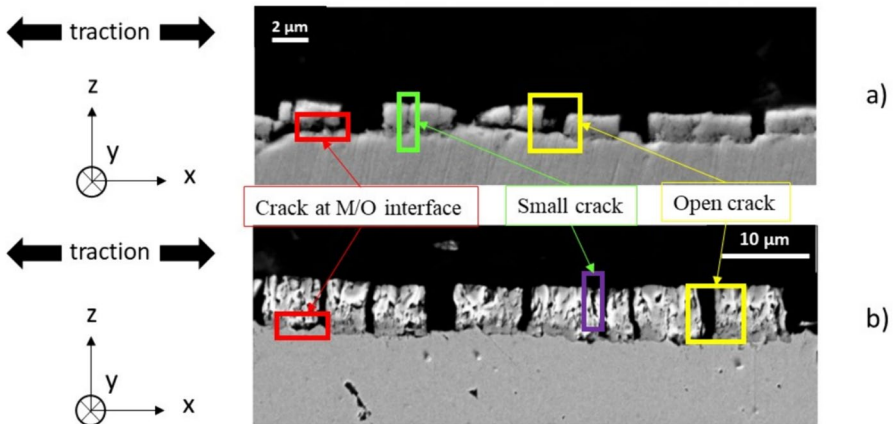


Fig. 4 SEM images of transverse section (after tensile fracture)—a Ni/NiO-1 μm and b Ni/NiO-6 μm

- Smaller cracks taking place either through the oxide or located near the surface of the oxide,
- Cracks situated between the oxide scale and the substrate.

Based on the crack morphology, two propagation modes prevailed: mode I (crack opening), in which cracks are perpendicular to the metal/oxide interface, and mode II, i.e., shearing along the metal/oxide interface. Spalling noticed for Ni/NiO-1 μm probably ensues from shearing along the metal/oxide interface that results in scale spalling.

EA Results

First, the amplitude of AE signals recorded during the tests were superimposed on the tensile curves to compare emissivity levels between configurations (Fig. 5). Very few signals were obtained for pure nickel: Only 28 signals remained after the pretreatments. These signals had a maximum amplitude that remained lower than 70 dB. The number of signals for Ni/NiO-1 μm was 730 times higher than the number recorded for pure nickel, with a maximum amplitude lower than 60 dB. Finally, around 49,800 signals were acquired for Ni/NiO-6 μm : The number of signals for Ni/NiO-6 μm was thus 2.5 times higher than the number of signals found for Ni/NiO-1 μm . The signals detected for Ni/NiO-6 μm had large amplitude as most of the signals had an amplitude larger than 60 dB. These comparisons between pure nickel, Ni/NiO-1 μm and Ni/NiO-6 μm highlighted the fact that oxidized specimens exhibited higher emissivity than non-oxidized specimens. It means that the AE activity detected in the oxidized specimens mainly originated from the oxide scale. As a consequence, for the oxidized specimens, there is no need to search for signals linked to mechanisms solely linked to the substrate.

Then, changes in cumulative absolute energy, which stands for the intensity of the signals during the tensile test, were sought (Fig. 6). There were curve breaking points in both configurations: For Ni/NiO-1 μm , there was a major increase in the cumulative absolute energy between 1.9 and 12% strain while this interval spanned from 1.9 to 9% strain for Ni/NiO-6 μm . Based on SEM observations, both interval spans matched the beginning of cracking to crack saturation. For Ni/NiO-1 μm ,

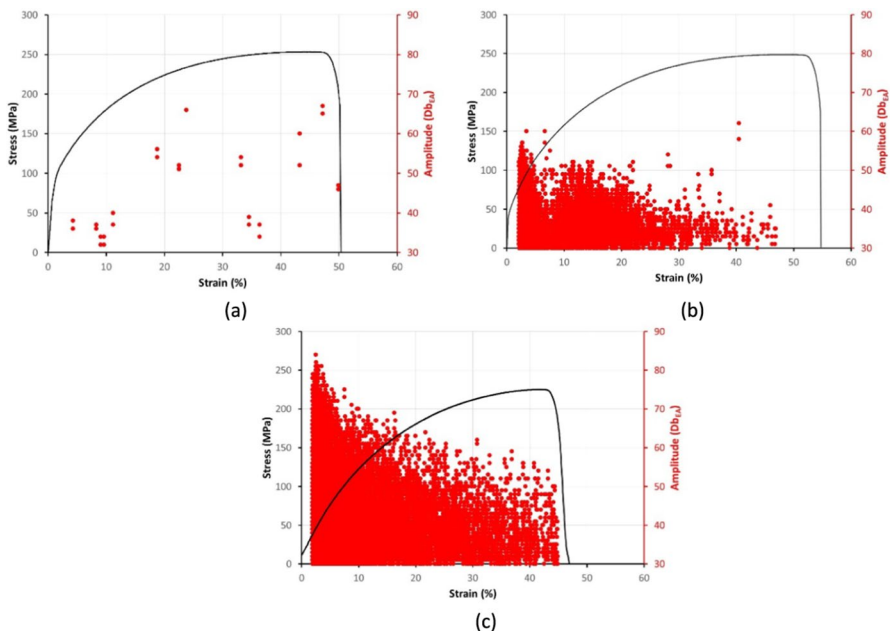


Fig. 5 AE amplitude versus tensile strain. **a** Ni, **b** Ni/NiO-1 μm and **c** Ni-NiO-6 μm

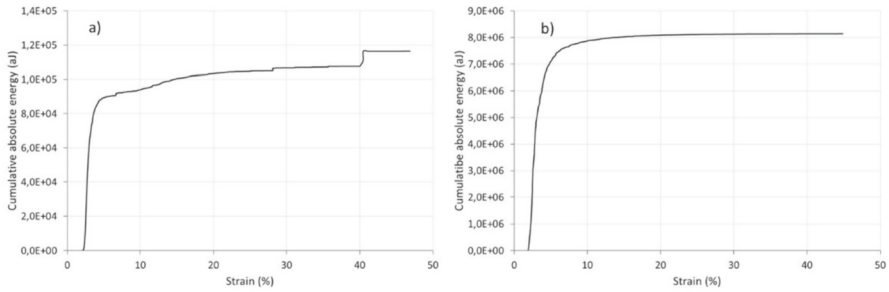


Fig. 6 Cumulative absolute energy versus tensile strain for **a** Ni/NiO-1 μm and **b** Ni/NiO-6 μm

spalling was also found to take place inside the identified interval. The observation of the cumulative energy changes did not lead to differentiate signals caused by cracking from signals linked to spalling. However, it confirmed the good detection of the deformation level at which first cracking occurred as identified using SEM observations.

Clusters of signals were then searched through the observations of different AE parameters. Figure 7 shows the evolution of the count number as a function of amplitude, as well as the duration as a function of absolute energy for both configurations. The observation of the count number–amplitude graph led to the identification of signals that stood out from the main cluster having a wavelike shape. These signals tend to have large count numbers (between 30 and 200)

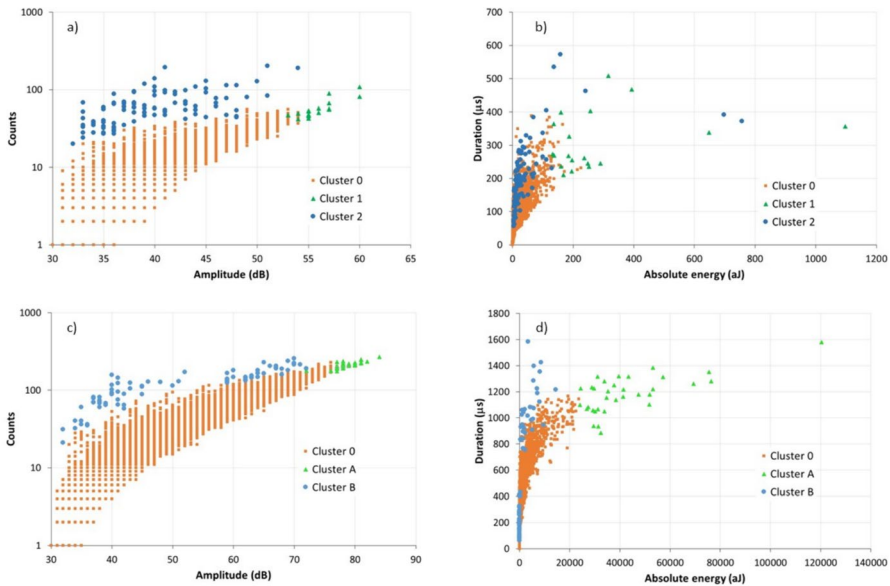


Fig. 7 Identification of clusters using hit number versus amplitude for **a** Ni/NiO-1 μm , **c** Ni/NiO-6 μm and hit duration versus absolute energy for **b** Ni/NiO-1 μm , **d** Ni/NiO-6 μm

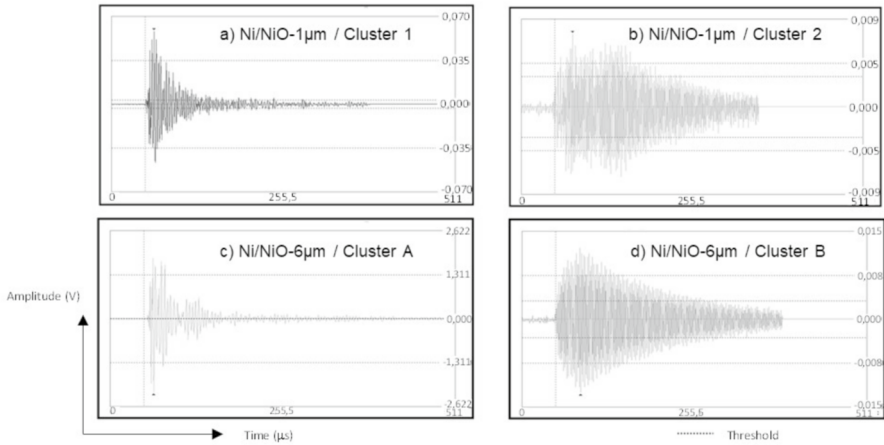


Fig. 8 Comparison of waveforms for the identified clusters. **a** Cluster 1 for Ni/NiO-1 µm, **b** cluster 2 for Ni/NiO-1 µm, **c** cluster A for Ni/NiO-6 µm, **d** cluster B for Ni/NiO-6 µm

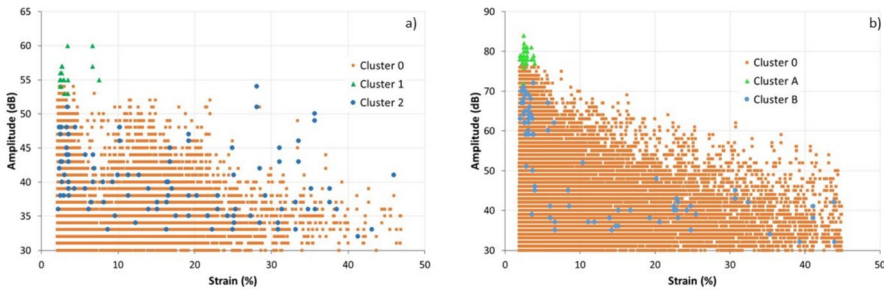


Fig. 9 AE amplitude versus tensile strain for **a** Ni/NiO-1 µm, **b** Ni/NiO-6 µm

and rather low amplitudes. This first group of signals is called cluster 1 for Ni/NiO-1 µm and cluster A for Ni/NiO-6 µm. Similarly, the use of the duration versus absolute energy graph led to find signals that split off from the main cluster, forming a small second branch. This second group gathers signals of high amplitude. This second group of signals is called cluster 2 for Ni/NiO-1 µm and cluster B for Ni/NiO-6 µm.

To check the relevance of the proposed clusters, the corresponding waveforms were observed. Representative waveforms are shown in Fig. 8 for each identified cluster. For each configuration, there are clear differences of waveforms between the identified clusters. The waveforms of clusters 1 and A have short duration time but high amplitude, whereas the waveforms of cluster 2 and B have lower global amplitude but tend to be noisier, with longer duration time.

The occurrence of the signals during the test (Fig. 9) was then used to try to link the clusters of signals to mechanisms:

- The signals of cluster 1 took place from a strain of 2.2 to 7.5% while the signals of cluster A spread from 1.9 to 3.9%.
- The signals of cluster 2 were spotted from a strain of 2.2% until fracture while the signals of cluster B were detected from a strain of 2% until fracture.

According to SEM images, for Ni/NiO-1 μm , signals of Class 1 could be linked to the larger cracks that are perpendicular to the interface. Signals of Class 2 could be linked to spalling: SEM images enabled spalling to be observed from 8.6% to fracture. The difference of strain between the detection between SEM images and AE could be explained by the fact that mode II propagation could be active prior to spalling observation. However, no spalling was detected for Ni/NiO-6 μm and it was shown that clusters 2 and B shared similar characteristics. In both configurations, cracks parallel to the interface, linked to mode II fracture propagation, were observed. As a consequence, cluster 2 and cluster B could be linked to this second type of cracks.

Discussion

To the best of the authors' knowledge, few articles dealt with the link between the characteristics of AE signals and the fracture propagation modes in oxide layers. However, several authors [24–27] associated high-energy AE hits with cracking initiation and propagation. This link was established in several study cases: the investigation of the effects of thermal cycling on steel oxide scale cracking [24], the study of creep loading effects on nickel oxide [25], the examination of cracking and spalling of Cr_2O_3 scale formed on Ni-30Cr alloy [26] or else the detection of breakaway oxidation during zirconium oxide growth [27]. Among the previous studies, two of them [24, 25] also linked AE hits of small amplitudes to spalling. Gaillet et al. [25] also specified that those low-energy hits associated with buckling and spalling had large duration time. These results are thus in agreement with the proposed conclusions. However, it is worth noting that Huang et al. [4] linked AE events having very high amplitudes to oxide delamination and spalling, whereas events of high amplitude were associated with cracking perpendicular to the oxide/substrate interface, when they examined the tensile failure of steam-side oxide scales formed on superheater tubes. The available data in the article do not allow to conclude on this difference. Nonetheless, the transverse sections of the oxide scales given by Huang et al. showed thick scales (around 50 μm) with very few local defects compared to the oxide scales observed in our study. This difference may explain why Huang et al. found that mode II crack propagation was associated with higher-energy events than mode I crack propagation.

Conclusion

Multiple cracking tests were performed using tensile tests associated with AE analysis in a SEM chamber. The aim was to improve the understanding and quantitative description of the damage behavior of oxide scale/substrate systems by correlating

crack propagation modes with acoustic signals. Two oxide scale thicknesses were examined in the Ni/NiO system: 1 and 6 μm . Whatever the oxide scale thickness, it was found that the first damages caused by tensile loading corresponded to through-scale cracks that were perpendicular to the oxide/metal interface. There was a multiplication of these cracks with the increase in the tensile strain until saturation occurred. Before saturation, mode II crack propagation also took place leading to local spalling in Ni/NiO-1 μm contrary to Ni/NiO-6 μm in which no spalling was observed.

The coupling of SEM observations with AE analysis led to correlate crack propagation modes with specific acoustic events. It was found that mode I crack propagation was associated with signals having high amplitude and high absolute energy, whereas less energetic AE events with long duration time were related to mode II crack propagation leading to possible spalling.

Author Contribution S.H. planned and performed the experiments, and analyzed the data from SEM. J.F. analyzed the AE data and wrote the original draft. J.M. and J.F. conceived the idea and supervised the project. J.M. offered technical guidance and reviewed the manuscript.

Data Availability No datasets were generated or analyzed during the current study.

Declarations

Conflict of interest The authors declare that they have no known competing financial interests or personal relationships that could have appeared to influence the work reported in this paper.

References

1. N. Godin, S. Huguet, R. Gaertner, and L. Salmon, *NDT & E International* **37**, 2004 (253–264).
2. W. Zhou, W. Zhao, Y. Zhang, and Z. Ding, *Composite Structures* **195**, 2018 (349–358).
3. M. G. R. Sause, F. Haider, and S. Horn, *Surface and Coatings Technology* **204**, 2009 (300–308).
4. J. L. Huang, K. Y. Zhou, X. M. Wang, Y. Y. Tu, and J. Q. Xu, *Journal of Applied Physics* **116**, 2014 (044907).
5. C. Bruns and M. Schütze, *Oxidation of Metals* **55**, 2001 (35–68).
6. D. L. Merson, D. I. Panyukov, M. A. Vyboishchik, and A. A. Razuvaev, *Russian Journal of Nondestructive Testing* **38**, 2002 (498–507).
7. M. M. Nagl, W. T. Evans, D. J. Hall, and S. R. J. Saunders, *Oxidation of Metals* **42**, 1994 (431–449).
8. Ogawa K, Ito K, Shoji T, Seo DW, Tezuka H, Kato H, Effects of Ce and Si additions to CoNiCrAlY bond coat materials on oxidation behavior and crack propagation of thermal barrier coatings. In: *Proc. Int. Therm. Spray Conf.*, Springer, 2006:640–651.
9. B. Picqué, P. O. Bouchard, P. Montmitonnet, and M. Picard, *Wear* **260**, 2006 (231–242).
10. L. Wang, C. G. Liu, X. H. Zhong, Y. X. Zhao, H. Y. Zhao, J. S. Yang, S. Y. Tao, and Y. Wang, *Journal of Thermal Spray Technology* **24**, 2015 (296–308).
11. T. Ganne, J. Crépin, S. Serror, and A. Zaoui, *Acta Materialia* **50**, 2002 (4149–4163).
12. D. Almond, M. Moghisi, and H. Reiter, *Thin Solid Films* **108**, 1983 (439–447).
13. M. Schütze, *Oxidation of Metals* **24**, 1985 (199–232).
14. D. J. Hall, S. Booth, and W. T. Evans, *Materials Science and Technology* **6**, 1990 (53–55).
15. Standard NF EN 1330-9; 2017.
16. M. M. Nagl, S. R. J. Saunders, W. T. Evans, and D. J. Hall, *Corrosion Science* **35**, 1993 (965–977).
17. J. Djuidje-Dzungam, C. Berdin, M. Andrieux, and P. Ribot, *Engineering Fracture Mechanics* **214**, 2019 (378–389).
18. C. Xie and W. Tong, *Acta Materialia* **53**, 2005 (477–485).

19. X. C. Zhang, C. J. Liu, F. Z. Xuan, Z. D. Wang, and S. T. Tu, *Computational Materials Science* **50**, 2010 (246–252).
20. F. L. Chen, X. He, P. A. Prieto-Munoz, and H. M. Yin, *International Journal of Plasticity* **67**, 2015 (171–191).
21. A. P. McGuigan, G. A. D. Briggs, V. M. Burlakov, M. Yanaka, and Y. Tsukahara, *Thin Solid Films* **424**, 2003 (219–223).
22. M. S. Hu and A. G. Evans, *Acta Materialia* **37**, 1989 (917–925).
23. F. Ahmed, K. Bayerlein, S. M. Rosiwal, M. Göken, and K. Durst, *Acta Materialia* **59**, 2011 (5422–5433).
24. W. Christl, A. Rahmel, and M. Schütze, *Materials Science and Engineering* **87**, 1987 (289–293).
25. L. Gaillet, S. Benmedakhene, A. Laksimi, and G. Moulin, *Journal of Materials Science* **38**, 2003 (1479–1484).
26. Y. Zhang and D. A. Shores, *Oxidation of Metals* **40**, 1993 (529–553).
27. V. Parry, M. T. Tran, and Y. Wouters, *Oxidation of Metals* **79**, 2013 (279–288).

Publisher's Note Springer Nature remains neutral with regard to jurisdictional claims in published maps and institutional affiliations.

Springer Nature or its licensor (e.g. a society or other partner) holds exclusive rights to this article under a publishing agreement with the author(s) or other rightsholder(s); author self-archiving of the accepted manuscript version of this article is solely governed by the terms of such publishing agreement and applicable law.